Journal of Materials Chemistry A

COMMUNICATION

View Article Online
View Journal | View Issue

Cite this: J. Mater. Chem. A, 2019, 7, 4383

Received 30th November 2018
Accepted 31st January 2019

DOI: 10.1039/c8ta11525g

rsc.li/materials-a

Creating ultrathin amorphous metal hydroxide and oxide nanosheet libraries†

Binbin Jia, Rui Hao, Zhongning Huang, Pengfei Hu, Lidong Li,* Yan Zhang and Lin Guo*

Designing a general strategy for synthesizing a series of 2D amorphous nanomaterials for emerging applications has become more and more fascinating and necessary. Herein, we report a general sacrificial template strategy which yields a library of 10 distinct 2D ultrathin amorphous metal hydroxide nanosheets, including mono-metal hydroxide nanosheets, binary-metal hydroxide nanosheets and ternary-metal hydroxide nanosheets. The key issue of synthesis is focused on the balance between the etching rate of the Cu_2O template and deposition rate of the metal hydroxide. Through a simple thermal treatment of the metal hydroxide precursors in an argon atmosphere, the corresponding amorphous porous metal oxide nanosheets can be easily obtained. This general method provides predictable pathways to synthesize 2D amorphous materials that are otherwise inaccessible.

Two dimensional (2D) materials,[1–7] especially metal hydroxides[8–10] and metal oxides,[11–13] as the representative types of 2D materials, have extensively attracted interest in fundamental research. In general, the undesired defects of 2D materials have huge impacts on the application of electronic devices and other fields.[14–16] However, the existence of defects in some fields can help to improve their novel properties.[17–19] It has been proved that the increase of defects is more conducive to improve the performance of electrocatalysts and supercapacitors due to their more defects and dangling bonds.[20–22] Therefore, increasing attention has been focused on taking various approaches to synthesize 2D amorphous materials.

Generally, compared to 2D crystalline materials, 2D films at the amorphous state are isotropic, lacking grain boundaries while possessing more defects and dangling bonds, which would give some special physical and chemical properties. 2D amorphous metal hydroxide and oxide materials[23] have many advantages over crystalline ones in the applications of batteries,[24] electrocatalysis[25] and supercapacitors.[26] For example, Jin *et al.* developed amorphous cobalt–iron hydroxide (CoFe–H) nanosheet electrocatalysts for the oxygen evolution reaction (OER) through a facile electrodeposition method. Due to their amorphous nature and large surface area, the amorphous CoFe–H nanosheets show excellent OER electrocatalytic performance compared to other state-of-the-art OER electrocatalysts.[27]

At present, researchers have witnessed success in preparing amorphous 2D hydroxide and oxide nanosheets, including $Ni(OH)_2$,[28] $Fe_{100-y-z}Co_yNi_zO_x$,[29] Fe–Co oxide nanosheets,[30] amorphous CoV-UAH,[31] MoO_2,[32] Cr_2O_3[33] and $LiFePO_4$.[34] Most amorphous 2D hydroxide and oxide nanosheets reported are formed by electrodeposition, photochemical deposition, $NaBH_4$ reduction, sputtering and thermal decomposition of metal precursors. It is still a great challenge to find an effective strategy to prepare a series of amorphous 2D hydroxide and oxide nanosheets. A template-assisted route has been developed and it have been proved to be an effective strategy for synthesizing 3D hydroxide nanocages.[35] Inspired by this method, herein, we report a general sacrificial strategy for controlled synthesis of 2D metal hydroxide and oxide nanosheets with an amorphous structure.

In this paper, Cu_2O nanosheets[36] were employed as a sacrificial template to promote the 2D planar growth of metal hydroxides into a nanosheet structure. By ligand etching between Cu_2O and $S_2O_3^{2-}$, various 2D hydroxide nanosheets can be synthesized, including mono-metal hydroxide nanosheets ($Co(OH)_2$, $Mg(OH)_2$, $Zn(OH)_2$, $Mn(OH)_2$/MnOOH, and $Fe(OH)_3$), binary-metal hydroxide nanosheets ($Co_xZn_y(OH)_{x+y}$, $Co_xFe_y(OH)_w$, $Co_xMg_y(OH)_{x+y}$, and $Co_xMn_y(OH)_w$) and ternary-metal hydroxide nanosheets ($Co_xMn_yFe_z(OH)_w$). Afterwards, through a simple thermal treatment in an argon atmosphere, the corresponding porous amorphous oxide nanosheets can be easily prepared, such as CoO, MgO, ZnO, MnO_x, and Fe_2O_3. Furthermore, in order to demonstrate the advantages of amorphous materials in some fields, the amorphous $Co(OH)_2$

School of Chemistry, Beijing Advanced Innovation Center for Biomedical Engineering, Beijing 100191, China. E-mail: guolin@buaa.edu.cn; lilidong@buaa.edu.cn

† Electronic supplementary information (ESI) available: Full experimental procedures, detailed structure description and other experimental results. See DOI: 10.1039/c8ta11525g

nanosheets were selected as an OER catalyst. The OER test indicates that the as-synthesized amorphous $Co(OH)_2$ nanosheets possess remarkable catalytic activity and stability with a low overpotential of 0.267 V at 10 mA cm^{-2}, a low Tafel slope of 34.4 mV dec^{-1} and a long operation time (8 h) in an alkaline environment compared to their crystalline counterparts and most Co-based nanomaterials.

The key issue of the synthesis is based on the balance between the etching rate of the Cu_2O template and deposition rate of the metal hydroxide. Therefore, the solution should always be in a relatively alkaline state. Due to easy particle aggregation during the process of releasing OH^- ions, it is necessary to select some hydroxides with the precipitate pH ranging from 7 to 12. Thus, $CoCl_2$, $MgCl_2$, $ZnCl_2$, $MnCl_2$, and $FeCl_2$ were chosen as the precursors in this experiment and the K_{sp} data are shown in Table S1.† The general synthesis route of amorphous 2D hydroxide nanosheets is illustrated in Fig. 1. Firstly, Cu_2O nanosheets were prepared *via* a hydrothermal reaction (Fig. S1†). Secondly, Cu_2O nanosheets were dispersed in solutions by ultrasonication. Meanwhile, metal salts were added to Cu_2O suspensions and homogenous suspensions were obtained by stirring to ensure the complete adsorption of metal ions (M^{x+}) onto the surfaces of Cu_2O nanosheets. Thirdly, $S_2O_3^{2-}$ ions were slowly added to the mixed solutions through a constant pressure titration funnel. During this process, $S_2O_3^{2-}$ ions were introduced into the reaction system, which can be driven by their chemical affinity to gather around the Cu_2O surface. At this moment, OH^- ions would be released when $S_2O_3^{2-}$ ions etched Cu_2O nanosheets. When the concentrations of OH^- ions increased to the precipitation threshold, $M(OH)_x$ started precipitating and the sheet-structure preferred forming around the etching interface. These factors guaranteed the geometry of Cu_2O nanosheets was perfectly preserved. Finally, the precipitates were washed and collected by centrifugation and 2D amorphous $M(OH)_x$ nanosheets were successfully obtained.

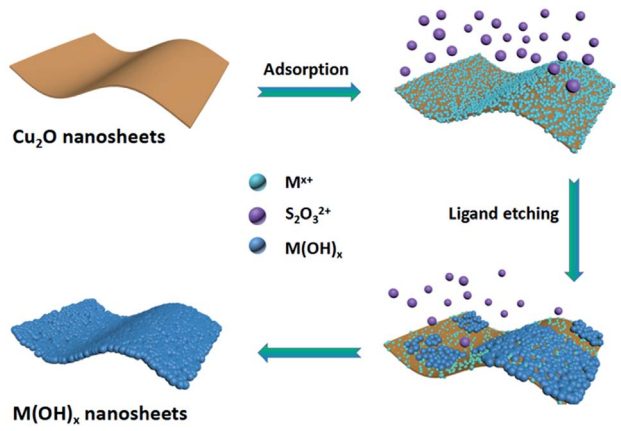

Fig. 1 The schematic illustration of the synthesis of amorphous metal hydroxide nanosheets ($M(OH)_x$ = $Co(OH)_2$, $Mg(OH)_2$, $Zn(OH)_2$, $Mn(OH)_x$, $Fe(OH)_3$, $Co_xZn_y(OH)_{x+y}$, $Co_xFe_y(OH)_w$, $Co_xMg_y(OH)_{x+y}$, $Co_xMn_y(OH)_w$, and $Co_xMn_yFe_z(OH)_w$).

The morphologies of the 2D nanosheets were characterized by scanning electron microscopy (SEM) (Fig. S2†) and transmission electron microscopy (TEM) (Fig. 2a–e), as shown in Fig. 2. The results revealed that a series of nanosheets were successfully prepared by the sacrificial template method, with uniform micrometer-size, and all of the nanosheets possessed an ultrathin structure and a similar morphology to that of the template. Interestingly, this method can make amorphous metal hydroxide nanosheets, while the original structures were layered ($Co(OH)_2$, $Zn(OH)_2$, $Mn(OH)_x$, and $Fe(OH)_3$) or non-lamellar structures ($Mg(OH)_2$) in their bulk crystals. The selected area electron diffraction (SAED) patterns in Fig. 2a–e display its amorphous nature, which is consistent with the results of X-ray diffraction (XRD) patterns (Fig. S3†). To give detailed morphological and structural information, HRTEM images are shown in Fig. $2a_1$–e_1. No lattice fringes are observed for the five samples, which further proves their amorphous structure. The corresponding elemental mapping results exhibit a homogeneous distribution of the M (Co, Zn, Mg, Mn, and Fe) and O elements throughout the whole hydroxide nanosheets (Fig. S4†). All of the above results prove that this is a generalized and effective approach to fabricate 2D amorphous hydroxide nanosheets. In addition, atomic force microscopy (AFM) was conducted to determine the thickness of 2D amorphous hydroxide nanosheets. As shown in Fig. $2a_2$–e_2 and a_3–e_3, the thickness of the nanosheets ranges from 1.4 nm to 2.7 nm (Table S2†).

To characterize the electronic structure of samples, X-ray photoelectron spectroscopy (XPS) was conducted, and the

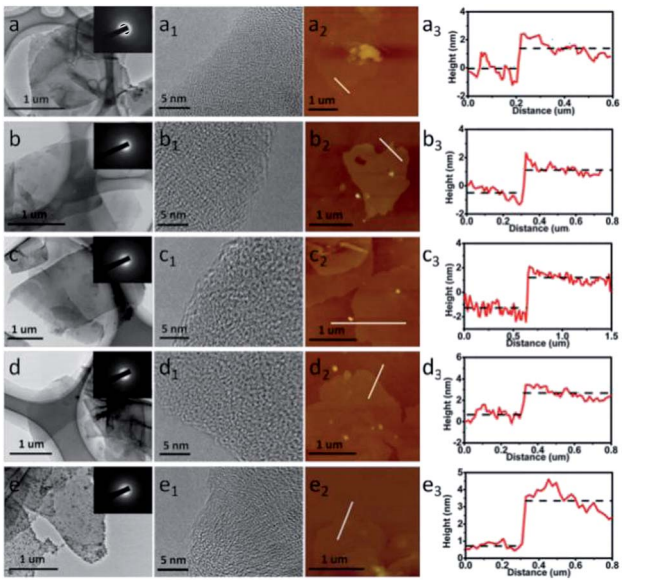

Fig. 2 (a–e) TEM, HRTEM and AFM images of amorphous metal hydroxide nanosheets ((a) $Co(OH)_2$, (b) $Zn(OH)_2$, (c) $Mg(OH)_2$, (d) $Mn(OH)_x$, and (e) $Fe(OH)_3$ (the inset of images show the corresponding selected-area electron-diffraction pattern of each sample)), (a_1–e_1) HRTEM images of amorphous metal hydroxide nanosheets ((a) $Co(OH)_2$, (b) $Zn(OH)_2$, (c) $Mg(OH)_2$, (d) $Mn(OH)_x$, and (e) $Fe(OH)_3$), and (a_2–e_2) and (a_3–e_3) the AFM images and AFM height images of amorphous metal hydroxide nanosheets ((a) $Co(OH)_2$, (b) $Zn(OH)_2$, (c) $Mg(OH)_2$, (d) $Mn(OH)_x$, and (e) $Fe(OH)_3$), respectively.

results are displayed in Fig. 3. $Co(OH)_2$ XPS spectra are shown in Fig. 3a and b. The core peaks for Co $2p_{3/2}$ and Co $2p_{1/2}$ located at 781.0 and 797.1 eV (Fig. 3a), respectively, which are characteristic features of Co^{2+}. Fig. 3b shows the XPS spectra and curve fitting results of O 1s, in which the stronger peak at 531.0 eV can be assigned to the OH^- ions, while the smaller peak at 533.0 eV can be ascribed to structural water.[37] Fig. 3c shows the XPS spectra of Zn $2p_{3/2}$ for the as-prepared sample. The peak at 1022.0 eV (Fig. 3c) can be ascribed to the Zn^{2+} in the hydroxide. The peak at 531.6 eV (Fig. 3d) can be assigned to the OH^- ions. To sum up, the component of this sample should be $Zn(OH)_2$.[38] The result of $Mg(OH)_2$ is similar to that of $Zn(OH)_2$ (the peak at 1303.5 eV (Fig. 3e) represents the Mg^{2+} and the peak at 531.6 eV (Fig. 3f) corresponds to OH^- ions).[13] However, the valence states of Mn and Fe have changed compared to those of their metal salts. The main peak at 641.8 eV in the Mn $2p_{3/2}$ spectrum should be assigned to Mn^{3+}, whose other peak is fitted at 643.1 eV, and the peak at 642.0 eV could be assigned to Mn^{2+} (Fig. 3g). Therefore, it can be inferred that two valence states of Mn ions are present in the sample. In Fig. 3h, an obvious fitted peak at 529.4 eV should have resulted from the lattice oxygen. The peaks at 530.5 eV and 530.9 eV can be assigned to two types of oxygen species integrated as "ions OH^-", associated with Mn^{2+} and Mn^{3+}, respectively. The peak at 532.4 eV can be assigned to the structural water.[35] The main peak at 711.4 eV and all the other fitted peaks in the Fe $2p_{3/2}$ spectrum (Fig. 3i) should be assigned to Fe^{3+}. In Fig. 3j, the enhanced peak at 529.4 eV also indicates the existence of Fe^{3+}. The peaks at 531.1 eV and 532.4 eV can be assigned to the "ions OH^-" and structural water, respectively.[39] To sum up, the valence state of Fe changed from +2 to +3 and some Mn^{2+} changed to Mn^{3+}, because the preformed $Fe(OH)_2$ or $Mn(OH)_2$ could be easily oxidized to $Fe(OH)_3$ or MnOOH by oxygen in the open reaction system. In addition, the XPS spectra of Cu 2p in the $M(OH)_x$ are provided in Fig S5,† It can see that there are some Cu components, which should have resulted from the adsorbed $Cu_2(S_2O_3)_x$, but the relative intensities of these elemental peaks are very low. In addition, the element content of Cu in the sample is very low, which is consistent with the results from the ICP of the sample (the atomic ratio of M and Cu tested by ICP are shown in Table S3†).

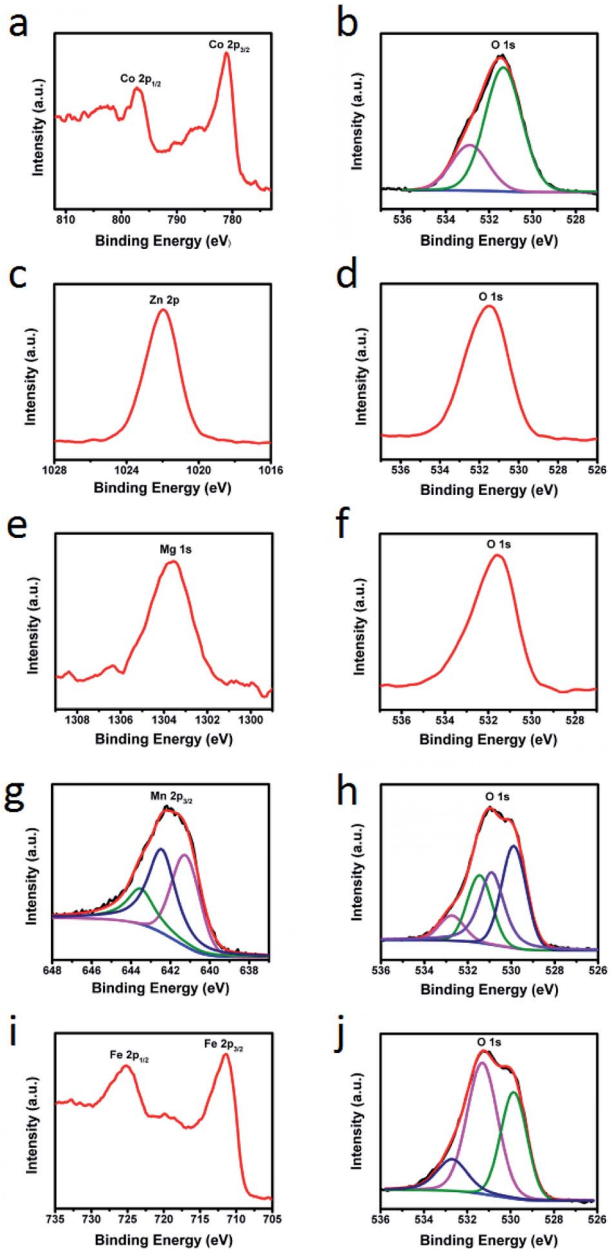

Fig. 3 XPS spectra of amorphous hydroxide nanosheets: (a and b) $Co(OH)_2$ (c and d) $Zn(OH)_2$, (e and f) $Mg(OH)_2$, (g and h) $Mn(OH)_2$/MnOOH, and (i and j) $Fe(OH)_3$.

In addition, the synthetic approach for the mono-metal hydroxide nanosheets can be easily extended to the synthesis of binary-metal hydroxide nanosheets and ternary-metal hydroxide nanosheets. Although binary-metal and ternary-metal hydroxides can be simply obtained, it is still difficult to precisely control their elemental composition because different elements have varied reaction kinetics and redox potentials. The $Co_xZn_y(OH)_w$ nanosheets with different atomic ratios are shown in Fig. S6a and b.† These nanosheets possess a similar morphology corresponding to that of Cu_2O nanosheets. The atomic ratios of Co and Zn tested by Inductively Coupled Plasma (ICP) are approximately 1 : 1 and 7 : 3, respectively. To demonstrate the versatility of the strategy for the fabrication of the binary-metal hydroxide nanosheets, amorphous $Co_xFe_y(OH)_{x+y}$, $Co_xMg_y(OH)_w$ and $Co_xMn_y(OH)_w$ nanosheets were also synthesized and the SEM images are shown in Fig. S7a–c.† The EDX mapping images showed a complete overlap of the corresponding elements which were homogeneously distributed on a sheet-like structure (Fig. S7†). Furthermore, a ternary-metallic amorphous $Co_xMn_yFe_z(OH)_w$ nanosheet was also synthesized based on the same strategy. The SEM image in Fig. S8† displays that the sample possess a sheet-like morphology. The molar ratio of Co, Mn and Fe in the $Co_xMn_yFe_z(OH)_w$ is about 7 : 1.5 : 1.5, as determined by ICP, which is consistent with the molar ratio of metal salts used in the synthesis. To reveal the spatial distribution of different elements in this unique nanostructure elemental mapping was performed and the results exhibited a homogeneous distribution of Co, Mn, Fe and O elements throughout the whole nanosheet.

The possible mechanism for the formation of the amorphous structure of metal hydroxides was suggested. It was thought to be mainly caused by non-uniform diffusion of OH^- ions. The $S_2O_3^{2-}$ ions could not be absorbed on the Cu_2O nanosheets at the same time, which made the etching rate of Cu_2O nanosheets inconsistent. Therefore, it could cause a small concentration gradient of OH^- ions at different locations of the nanosheet. When the OH^- ions were combined with metal ions, inhomogeneous diffusion could cause the formation of a large number of amorphous clusters. Moreover, the sizes of amorphous clusters could be controlled by adjusting the concentrations of ions and amorphous nanosheets with different thicknesses were generated. To prove our assumption, single-layer nanosheets with different thicknesses were obtained successfully by adjusting the concentrations of OH^- ions and metal ions, respectively. Taking amorphous $Co(OH)_2$ nanosheets as an example, the initial ultrathin amorphous $Co(OH)_2$ nanosheet was 1.4 nm thick (ua-$Co(OH)_2$), and when we doubled the concentration of all reactants, thicker amorphous $Co(OH)_2$ nanosheets (ta-$Co(OH)_2$) of 3.7 nm were obtained (Fig. S9†) and the nanosheets still retained their morphology and amorphous structure (Fig. S10†).

In addition to the amorphous metal hydroxide nanosheets, amorphous metal oxide nanosheets, especially 2D amorphous porous metal oxides, have also increasingly attracted attention due to their excellent performances in many fields. Moreover, a precise pore structure is highly desired, because it may have a significant effect on many fields, especially in enhancing battery performances. For example, the pore structure of 2D materials has been believed to effectively solve restacking problems and significantly shorten ion transmission distance as electrode materials.[40] Unfortunately, so far, few studies on the precisely controlled synthesis of 2D amorphous metal oxides have been reported. In our work, amorphous oxide nanosheets can be simply obtained through a dehydration reaction at 250 °C for only 1 hour and the corresponding Raman spectra are shown in Fig. S11† to confirm the chemical composition of the samples. As shown in Fig. 4 and S12,† five different amorphous porous monometallic oxide nanosheets (CoO, MgO, ZnO, MnO_x and Fe_2O_3) were obtained after thermal treatment of the corresponding hydroxide samples. The SEM and TEM images indicated that the oxide nanosheets basically retained the morphology and structure of the original hydroxide nanosheets. Meanwhile, their amorphous structures were identified by the corresponding selective area electron diffraction (SAED) (the insets of Fig. 4a–e) and XRD patterns (Fig. S13†). Due to desorption of moisture during the heating process, a large number of holey structures were generated (Fig. 4a_1–e_1) with the sizes of pores being approximately 5–7 nm. To give detailed morphological and structural information, HRTEM images were taken and are shown in Fig. 4a_2–e_2, showing disordered arrangement of atoms in the nanosheets which further proved their amorphous structure. The corresponding elemental mapping analyses (Fig. S14†) revealed that M (Co, Zn, Mg, Mn, and Fe) and O were homogeneously distributed across the whole nanosheets. AFM was conducted to determine the thickness of 2D amorphous hydroxide nanosheets. As shown in the (Fig. S15†), the thickness of nanosheets ranged from 1.5 nm to 2.7 nm (Table S4†). Prompted by their unique morphology, these 2D porous amorphous oxide nanosheets may be expected to show promising applications in electrochemical energy storage devices and gas sensors.

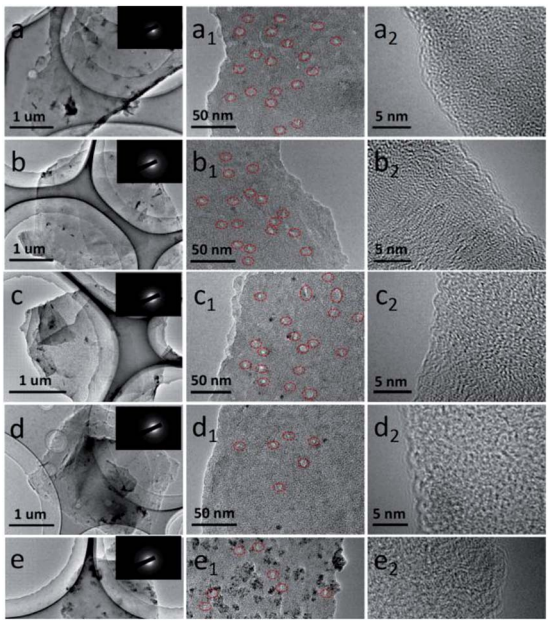

Fig. 4 (a–e and a_1–e_1) TEM images of amorphous metal hydroxide nanosheets ((a) CoO, (b) ZnO, (c) MgO, (d) MnO_x, and (e) Fe_2O_3) (the inset of images in a–e show the corresponding selected-area electron-diffraction patterns; the inset of red circles in a_1–e_1 show the mesoporous structure of amorphous metal oxide nanosheets). (a_2–e_2) HRTEM images of amorphous metal hydroxide nanosheets ((a) CoO, (b) ZnO, (c) MgO, (d) MnO_x, and (e) Fe_2O_3).

As a key reaction involved in various energy-conversion systems, the OER has been widely studied.[41,42] However, the development of efficient electrocatalysts still remains a daunting challenge, due to their high overpotential and poor durability. One way to improve the OER activity of electrocatalysts is to synthesize transition metal hydroxides with amorphous structures, because disordered structures can offer more active catalytic sites. Another effective approach is to develop 2D nanosheets, due to their more catalytically active sites and high interfacial contact area.[43–47] In order to demonstrate the performance advantage of our amorphous 2D materials, the OER electrocatalytic activity of three different samples: ua-$Co(OH)_2$ nanosheets, ta-$Co(OH)_2$ nanosheets and crystalline $Co(OH)_2$ nanosheets were evaluated in 1.0 M KOH solution by using a typical three-electrode cell. A glassy carbon electrode modified with the catalyst, an Ag/AgCl electrode and a Pt wire were used as the working electrode, reference electrode, and counter-electrode, respectively. Linear sweep voltammetry (LSV) curves of ua-$Co(OH)_2$, ta-$Co(OH)_2$ and crystalline $Co(OH)_2$ nanosheets are shown in Fig. 5a. It can be seen that amorphous $Co(OH)_2$ nanosheets possess an obviously lower onset potential than crystalline $Co(OH)_2$ nanosheets. The applied potential at a current density of 10 mA cm^{-2} was always used as a common

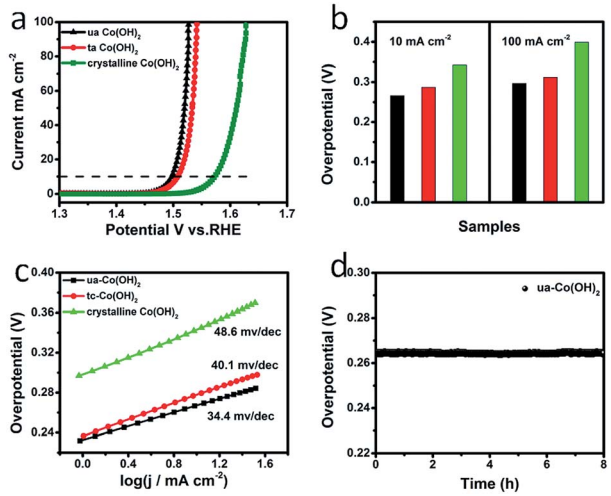

Fig. 5 (a) LSV curves, (b) the overpotential of ua-$Co(OH)_2$ nanosheets, ta-$Co(OH)_2$ nanosheets and crystalline $Co(OH)_2$ nanosheets at a current density of 10 mA cm^{-2} and 100 mA cm^{-2}, (c) Tafel plots of ua-$Co(OH)_2$ nanosheets, ta-$Co(OH)_2$ nanosheets and crystalline $Co(OH)_2$ nanosheets, and (d) chronopotentiometry curves of ua-$Co(OH)_2$ nanosheets at 10 mA cm^{-2}.

criterion to evaluate the OER activity. For the ua-$Co(OH)_2$, ta-$Co(OH)_2$ and crystalline $Co(OH)_2$ nanosheets, 1.496 V, 1.517 V and 1.572 V were needed to reach a current density of 10 mA cm^{-2}, corresponding to an overpotential of 266 mV, 287 mV and 342 mV, respectively. These are even comparable to the performance of many other Co-based catalysts (Table S3†), RuO_2 catalysts,[48] and IrO_2 catalysts[49] in 1.0 M KOH solution. Of note, when the current density of the ua-$Co(OH)_2$ and ta-$Co(OH)_2$ nanosheets increases to 100 mA cm^{-2} (Fig. 5b), the overpotentials have only a slight rise to 297 mV and 302 mV, respectively, which are much lower than those of crystalline $Co(OH)_2$ nanosheets (399 mV). Compared to ta-amorphous $Co(OH)_2$ nanosheets, ua-$Co(OH)_2$ nanosheets show higher electrocatalytic activity due to its larger specific surface area and more ultra-thin structure. Furthermore, the kinetics of the OER was examined by Tafel plots (Fig. 5c). The Tafel slopes of ua-$Co(OH)_2$ nanosheets (34.4 mV dec^{-1}) and ta-$Co(OH)_2$ nanosheets (40.1 mV dec^{-1}) are much smaller than that of crystalline $Co(OH)_2$ nanosheets (48.6 mV dec^{-1}) and other previously reported OER electrocatalysts (Table S3†). It should be pointed out that an amorphous CoO nanosheet also exhibits excellent catalytic activity with a low overpotential of 314 mV at 10 mA cm^{-2} and a low Tafel slope of 57.4 mV dec^{-1} (Fig. S16†). In addition, we also tested the long-term durability of ua-$Co(OH)_2$ nanosheet catalyst (Fig. 5d). No voltage decay could be detected for the ua-$Co(OH)_2$ nanosheet catalysts during the long-term testing. Compared to its crystalline counterparts, the structural benefits of the ua-$Co(OH)_2$ ultrathin nanosheet catalyst in OER catalysis can be summarized as follows: Firstly, the 2D ultrathin nature of the nanosheet endows larger solid–liquid interfacial area for ion interaction, thus facilitating the charge transport between nanosheets; secondly, the amorphous structure can induce abundant defects, which are responsible for the remarkably enhanced OER activity; finally, the structural flexibility can act as an effective buffer area for the volume change during reversible redox reactions, thus avoiding severe mechanical deformation or material swelling under continuous LSV operation.

Conclusions

In summary, by controlling the balance between the etching rate of the Cu_2O template and deposition rate of the metal hydroxide, we have developed a simple sacrificial template strategy to create ultrathin amorphous nanosheet libraries, including mono-metal hydroxide nanosheets, binary-metal hydroxide nanosheets, and ternary-metal hydroxide nanosheets. And amorphous metal oxide nanosheets with holey structures can be readily obtained by appropriate thermal treatment of the corresponding hydroxide nanosheets. The disordered atomic arrangement of the products can generate more active sites, which exhibit exceptional properties in various energy-related applications. As a demonstration, we evaluated amorphous $Co(OH)_2$ nanosheets prepared by our method as an OER catalyst and found superior performance in comparison with their crystalline counterparts and most Co-based nanomaterials.

Conflicts of interest

There are no conflicts to declare.

Acknowledgements

The authors acknowledge the financial support from the National Natural Science Foundation of China (51532001 and 51772011.

Notes and references

1 K. S. Novoselov, A. K. Geim, S. V. Morozov, D. Jiang, Y. Zhang, S. V. Dubonos, I. V. Grigorieva and A. A. Firsov, *Science*, 2004, **306**, 666.
2 A. E. Del Rio Castillo, V. Pellegrini, A. Ansaldo, F. Ricciardella, H. Sun, L. Marasco, J. Buha, Z. Dang, L. Gagliani, E. Lago, N. Curreli, S. Gentiluomo, F. Palazon, M. Prato, R. Oropesa-Nunez, P. S. Toth, E. Mantero, M. Crugliano, A. Gamucci, A. Tomadin, M. Polini and F. Bonaccorso, *Mater. Horiz.*, 2018, **5**, 890.
3 J. Park, M. Lee, D. W. Feng, Z. H. Huang, A. C. Hinckley, A. Yakoyenko, X. D. Zou, Y. Cui and Z. A. Bao, *J. Am. Chem. Soc.*, 2018, **140**, 10315.
4 D. Geng and G. Yu, *Mater. Horiz.*, 2018, **5**, 1021.
5 Z. Yin, H. Li, H. Li, L. Jiang, Y. Shi, Y. Sun, G. Lu, Q. Zhang, X. Chen and H. Zhang, *ACS Nano*, 2012, **6**, 74.
6 N. Parvin, Q. Jin, Y. Wei, R. Yu, B. Zheng, L. Huang, Y. Zhang, L. Wang, H. Zhang, M. Gao, H. Zhao, W. Hu, Y. Li and D. Wang, *Adv. Mater.*, 2017, **29**, 1606755.
7 M. Z. Rahman, C. W. Kwong, K. Davey and S. Z. Qiao, *Energy Environ. Sci.*, 2016, **9**, 709.

8 J. L. Gunjakar, I. Y. Kim, J. M. Lee, N. S. Lee and S. J. Hwang, *Energy Environ. Sci.*, 2013, **6**, 1008.
9 R. Ma, X. Liu, J. Liang, Y. Bando and T. Sasaki, *Adv. Mater.*, 2014, **26**, 4173.
10 Z. J. Zhu, H. J. Yin, C. T. He, M. Al-Mamun, P. R. Liu, L. X. Jiang, Y. Zhao, Y. Wang, H. G. Yang, Z. Y. Tang, D. Wang, X. M. Chen and H. J. Zhao, *Adv. Mater.*, 2018, **30**, 1801171.
11 Q. Qu, S. Yang and X. Feng, *Adv. Mater.*, 2011, **23**, 5574.
12 Z. Sun, T. Liao, Y. Dou, S. M. Hwang, M. S. Park, L. Jiang, J. H. Kim and S. X. Dou, *Nat. Commun.*, 2014, **5**, 3813.
13 H. Zhao, Y. Zhu, F. Li, R. Hao, S. Wang and L. Guo, *Angew. Chem., Int. Ed.*, 2017, **56**, 8766.
14 T. Stephenson, Z. Li, B. Olsen and D. Mitlin, *Energy Environ. Sci.*, 2014, **7**, 209.
15 P. Chen, K. Xu, T. Zhou, Y. Tong, J. Wu, H. Cheng, X. Lu, H. Ding, C. Wu and Y. Xie, *Angew. Chem., Int. Ed.*, 2016, **55**, 2488.
16 W. Guo, F. Zhang, C. Lin and Z. L. Wang, *Adv. Mater.*, 2012, **24**, 4761.
17 J. Xie, H. Zhang, S. Li, R. Wang, X. Sun, M. Zhou, J. Zhou, X. W. Lou and Y. Xie, *Adv. Mater.*, 2013, **25**, 5807.
18 H. Wang, J. Zhang, X. Hang, X. Zhang, J. Xie, B. Pan and Y. Xie, *Angew. Chem., Int. Ed.*, 2015, **54**, 1195.
19 F. Lei, Y. Sun, K. Liu, S. Gao, L. Liang, B. Pan and Y. Xie, *J. Am. Chem. Soc.*, 2014, **136**, 6826.
20 Y. Sun, S. Gao, F. Lei and Y. Xie, *Chem. Rev.*, 2015, **44**, 623.
21 Z. C. Wu, B. E. Li, Y. J. Xue, J. J. Li, Y. L. Zhang and F. Gao, *J. Mater. Chem. A*, 2015, **3**, 19445.
22 J. Xiong, J. Di, J. X. Xia, W. S. Zhu and H. M. Li, *Adv. Funct. Mater.*, 2018, **28**, 1801983.
23 H. W. Zhao, Y. H. Yue, Y. W. Zhang, L. D. Li and L. Guo, *Adv. Mater.*, 2016, **28**, 2037.
24 Y. Z. Jiang, D. Zhang, Y. Li, T. Z. Yuan, N. Bahlawane, C. Liang, W. P. Sun, Y. H. Lu and M. Yan, *Nano Energy*, 2014, **4**, 23.
25 J. Z. Liu, J. W. Nai, T. T. You, P. F. An, J. Zhang, G. S. Ma, X. G. Niu, C. Y. Liang, S. H. Yang and L. Guo, *Small*, 2018, **14**, 1703514.
26 H. B. Li, M. H. Yu, F. X. Wang, P. Liu, Y. Liang, J. Xiao, C. X. Wang, Y. X. Tong and G. W. Yang, *Nat. Commun.*, 2013, **4**, 1894.
27 W. Liu, H. Liu, L. N. Dang, H. X. Zhang, X. L. Wu, B. Yang, Z. J. Li, X. W. Zhang, L. C. Lei and S. Jin, *Adv. Funct. Mater.*, 2017, **27**, 1603904.
28 Y. Z. Su, K. Xiao, N. Li, Z. Q. Liu and S. Z. Qiao, *J. Mater. Chem. A*, 2014, **2**, 13845.
29 R. D. Smith, M. S. Prévot, R. D. Fagan, Z. P. Zhang, P. A. Sedach, M. K. J. Siu, S. Trudel and C. P. Berlinguette, *Science*, 2013, **340**, 60.
30 L. Z. Zhuang, L. Ge, Y. S. Yang, M. R. Li, Y. Jia, X. D. Yao and Z. H. Zhu, *Adv. Mater.*, 2017, **29**, 1606793.
31 J. Z. Liu, Y. F. Ji, J. W. Nai, X. G. Niu, Y. Luo, L. Guo and S. H. Yang, *Energy Environ. Sci.*, 2018, **11**, 1736.
32 W. Liu, Q. Xu, W. L. Cui, C. H. Zhu and Y. H. Qi, *Angew. Chem., Int. Ed.*, 2017, **56**, 1600.
33 Z. M. Hu, X. Xiao, H. Y. Jin, T. Q. Li, M. Chen, Z. Liang, Z. F. Guo, J. Li, J. Wan, L. Huang, Y. R. Zhang, G. Feng and J. Zhou, *Nat. Commun.*, 2017, **8**, 15630.
34 T. C. Liu, Y. C. Feng, Y. D. Duan, S. H. Cui, L. P. Lin, J. T. Hu, H. Guo, Z. Q. Zhuo, J. X. Zheng, Y. Lin, W. L. Yang, K. Amine and F. Pan, *Nano Energy*, 2015, **18**, 187.
35 J. W. Nai, Y. Tian, X. Guan and L. Guo, *J. Am. Chem. Soc.*, 2013, **135**, 16082.
36 S. Gao, Y. F. Sun, F. C. Lei, J. W. Liu, L. Liang, T. W. Li, B. C. Pan, J. F. Zhou and Y. Xie, *Nano Energy*, 2014, **8**, 205.
37 J. K. Chang, C. M. Wu and I. W. Sun, *J. Mater. Chem.*, 2010, **20**, 3729.
38 M. C. Biesinger, L. W. M. Lau, A. R. Gerson and R. S. C. Smart, *Appl. Surf. Sci.*, 2010, **257**, 887.
39 M. C. Biesinger, B. P. Payne, A. P. Grosvenor, L. W. M. Lau, A. R. Gerson and R. S. Smart, *Appl. Surf. Sci.*, 2011, **257**, 2717.
40 L. L. Peng, P. Xiong, L. Ma, Y. F. Yuan, Y. Zhu, D. H. Chen, X. Y. Luo, J. Lu, K. Amine and G. H. Yu, *Nat. Commun.*, 2017, **8**, 15139.
41 W. Liu, P. Rodriguez, L. Borchardt, A. Foelske, J. Yuan, A.-K. Herrmann, D. Geiger, Z. Zheng, S. Kaskel, N. Gaponik, R. Koetz, T. J. Schmidt and A. Eychmueller, *Angew. Chem., Int. Ed.*, 2013, **52**, 9849.
42 J. S. Chen, J. W. Ren, M. Shalom, T. Fellinger and M. Antonietti, *ACS Appl. Mater. Interfaces*, 2016, **8**, 5509.
43 R. D. L. Smith, M. S. Prevot, R. D. Fagan, Z. P. Zhang, P. A. Sedach, M. K. J. Siu, S. Trudel and C. P. Berlinguette, *Science*, 2013, **340**, 60.
44 R. D. L. Smith, M. S. Prevot, R. D. Fagan, S. Trudel and C. P. Berlinguette, *J. Am. Chem. Soc.*, 2013, **135**, 11580.
45 Y. W. Liu, C. Xiao, M. J. Lyu, Y. Lin, W. Z. Cai, P. C. Huang, W. Tong, Y. M. Zou and Y. Xie, *Angew. Chem., Int. Ed.*, 2015, **54**, 11231.
46 F. Song and X. L. Hu, *Nat. Commun.*, 2014, **5**, 4477.
47 A. Indra, P. W. Menezes, N. R. Sahraie, A. Bergmann, C. Das, M. Tallarida, D. Schmeisser, P. Strasser and M. Driess, *J. Am. Chem. Soc.*, 2014, **136**, 17530.
48 H. W. Huang, C. Yu, J. Yang, C. T. Zhao, X. T. Han, Z. B. Liu and J. S. Qiu, *ChemElectroChem*, 2016, **3**, 719.
49 Y. W. Tan, H. Wang, P. Liu, Y. H. Shen, C. Cheng, A. Hirata, T. Fujita, Z. Tang and M. W. Chen, *Energy Environ. Sci.*, 2016, **9**, 2257.

